

A central tidal disruption event candidate in high redshift quasar SDSS J000118.70+003314.0

Ying Gu, Xue-Guang Zhang^{*}, Xing-Qian Chen, Xing Yang, and En-Wei Liang[†]

*Guangxi Key Laboratory for Relativistic Astrophysics, School of Physical Science and Technology,
Guangxi University, Nanning 530004, People's Republic of China*

Accepted XXX. Received YYY; in original form ZZZ

ABSTRACT

We report a high-redshift ($z = 1.404$) tidal disruption event (TDE) candidate in SDSS J000118.70+003314.0 (SDSS J0001), which is a quasar with apparent broad Mg II emission line. The long-term variability in its nine-year photometric *ugriz*-band light curves, obtained from the SDSS Stripe82 and the PHOTOOBJALL databases, can be described by the conventional TDE model. Our results suggest that the TDE is a main-sequence star with mass of $1.905^{+0.023}_{-0.009} M_{\odot}$ tidally disrupted by a black hole (BH) with mass $6.5^{+3.5}_{-2.6} \times 10^7 M_{\odot}$. The BH mass is about 7.5 times smaller than the virial BH mass derived from the broad Mg II emission line, which can be explained by non-virial dynamic properties of broad emission lines from TDEs debris. Furthermore, we examine the probability that the event results from intrinsic variability of quasars, which is about 0.009%, through applications of the DRW/CAR process. Alternative explanations for the event are also discussed, such as the scenarios of dust obscurations, microlensing and accretion. Our results provide clues to support that TDEs could be detectable in broad line quasars as well as in quiescent galaxies, and to indicate the variability of some active galactic nuclei may be partly attributed to central TDEs.

Key words: galaxies: nuclei – quasars: emission lines – transients: tidal disruption events – quasars: individual (SDSS J0001)

1 INTRODUCTION

It is generally believed that massive galaxies host a central supermassive black hole (SMBH) (Kormendy & Gebhardt 2001; Kormendy & Ho 2013). A tidal disruption event (TDE) occurs when a supermassive black hole rips apart a passing star (Nolthenius & Katz 1982; Carter & Luminet 1983). TDEs are the best probes for studying the central SMBHs and corresponding accretion systems. They were theoretically predicted (Nolthenius & Katz 1982; Carter & Luminet 1983; Rees 1988) and were observationally confirmed (e.g. Bade et al. 1996; Komossa & Greiner 1999; Gezari 2021).

Theoretically, the TDE phenomenon was firstly predicted by Rees (1988) and Phinney (1989), who calculated the rate of fallback materials through numerical simulations and analytical methods by assuming a star completely destroyed by a SMBH. They have shown that approximately half of the star's mass can be captured and an accretion disk surrounding the SMBH is formed, leading to a bright flare event in the ultraviolet(UV)-optical and soft X-ray band (Rees 1988; Phinney 1989; Kochanek 1994; Guillochon et al. 2014). Ivanov & Novikov (2001); Kobayashi et al. (2004) have proposed that TDEs should exhibit more complex behavior and partial disruption of stars is likely more common than the complete disruption. The numerical studies by Rosswog et al. (2009); Lodato et al. (2009) have given the time-dependent fallback rate for varying polytropic spheres with index γ . The simulations by Guillochon & Ramirez-Ruiz (2013)

show further effects of varying impact parameter β on the time-dependent fallback rate in cases ranging from no mass loss to deeply penetrating encounters. Based on these theoretical results, the following two basic points can be obtained. First, a unique time-dependent brightness decay pattern of $\sim t^{-5/3}$ is a common feature of optical TDEs at late times. Meanwhile, some studies have shown deviations from this pattern at early times after the time of peak brightness such as Lodato & Rossi (2011); Guillochon & Ramirez-Ruiz (2013). Second, BH mass should be limited to be smaller than $\sim 10^8 M_{\odot}$ (the Hills limits), otherwise the star should be totally swallowed by the central SMBH before being tidally disrupted, unless the central SMBH spin is extremely fast (Kesden 2012). Guillochon et al. (2014) (the known TDEFIT code) have performed a hydrodynamical simulation to investigate the structures and the dynamical evolutions of the debris stream formed from the tidal disruption of a main-sequence star. Additionally, Mockler et al. (2019) have added the TDE modular to the known MOSFIT code. More recent reviews on theoretical simulations of TDEs can be found in Stone et al. (2019).

Observationally, TDE candidates were first detected by the ROSAT satellite in the soft X-ray band (Komossa & Bade 1999; Grupe et al. 1999; Greiner et al. 2000). Thereafter, similar X-ray TDE candidates were also detected by other space X-ray missions, including the XMM-Newton observatory, Chandra X-ray observatory, and Swift/X-Ray Telescope (Donley et al. 2002; Esquej et al. 2007, 2008; Cappelluti et al. 2009; Maksym et al. 2014; Lin et al. 2015; Saxton et al. 2017, 2021). In addition to these X-ray TDEs, three on-axis jetted TDEs were discovered by the Neil Gehrels Swift Observatory: Swift J1644+57 (Bloom et al. 2011; Burrows et al. 2011; Levan et al. 2011), Swift J2058.4+0516 (Cenko et al. 2012) and

^{*} E-mail: xgzhang@gxu.edu.cn

[†] E-mail: lew@gxu.edu.cn

Swift J1112.28238 (Brown et al. 2015). In addition, the most recent jetted TDE AT 2022cmc was discovered by an optical sky survey (Andreoni et al. 2022; Pasham et al. 2023; Yao et al. 2024). A recent review on the fraction of TDEs that launch jets can be found in De Colle & Lu (2020). Due to our main focus on optical TDEs, there is no further discussion on X-ray TDEs in the manuscript.

Thanks to the high-quality light curves provided by the public sky survey projects in optical bands, more and more optical TDEs have been reported through unique spectroscopic features and/or through long-term variability properties of TDEs. Descriptions of one to two known TDE candidates from each current sky survey are given as follows. Through SDSS (Sloan Digital Sky Survey) (Almeida et al. 2023) catalog of galaxies, several TDE candidates have been reported by Komossa et al. (2008); Yang et al. (2013) due to the discovered coronal lines. Meanwhile, through SDSS provided long-term photometric datasets in Stripe82 (Frieman et al. 2008), SDSS-TDE1 and SDSS-TDE2 have been reported in van Velzen et al. (2011). Through CSS (Catalina Sky Survey) (Drake et al. 2009), one known optical TDE candidate has been reported in CSS100217:102913+404220 in Drake et al. (2011). Through OGLE (Optical Gravitational Lensing Experiment) (Udalski et al. 2015; Wyrzykowski et al. 2014), the optical TDE OGLE17aaj has been reported in Gromadzki et al. (2019); Wyrzykowski et al. (2017); Kajava et al. (2020). Through ASAS-SN (All Sky Automated Survey for supernovae) (Shappee et al. 2014), ASASSN-14ae and ASASSN-15lh have been reported in Holoien et al. (2014); Leloudas et al. (2016); Wevers et al. (2019). Through Pan-STARRS (Panoramic Survey Telescope & Rapid Response System) medium-deep survey (Chambers 2007), the known optical TDEs PS1-10jh and PS1-11af have been reported by Gezari et al. (2012); Chornock et al. (2014). Through PTF (Palomar Transient Factory) (Law et al. 2009), the optical TDE PTF09ge has been reported by Arcavi et al. (2014). Additionally, through ATLAS (Asteroid Terrestrial-impact Last Alert System) (Tonry et al. 2018), a faint and fast TDE in a quiescent Balmer strong Galaxy ATLAS18mlw was reported in Hinkle et al. (2023). Through ZTF (Zwicky Transient Facility) (Bellm et al. 2019), TDE AT2018zr/PS18kh have been reported by van Velzen et al. (2019). The number of detected optical TDEs is increasing quickly. More than 100 optical TDE candidates have been reported in the literature (see the collected TDE candidates listed in <https://tde.space/>). The TDEs are rare and the rate is $\sim 10^{-4} - 10^{-5}$ year $^{-1}$ galaxy $^{-1}$ (Wang & Liu 2016; Stone & Metzger 2016). Recently, several samples of TDE candidates have been identified, such as TDE candidates reported in Sazonov et al. (2021) from the eROSITA/SRG all-sky survey, and in van Velzen et al. (2021); Hammerstein et al. (2023) and Yao et al. (2023) from ZTF. The optical-UV properties of TDEs are discussed in van Velzen et al. (2021). More recent reviews on observational properties of optical TDE candidates can be found in Gezari (2021).

Besides the discussed photometric variability properties related to TDEs, spectroscopic properties of TDEs are discussed as follows. The optical spectra of TDEs can be roughly classified into three spectroscopic types in van Velzen et al. (2021), (1): TDE-H type, which has broad H α and H β emission lines; (2): TDE-H+He, which is characterized by broad emission lines for H α and H β , a complex of emission lines around He II λ 4686, and often includes emission at N III λ 4640 and λ 4100. Additionally, some cases exhibit emission at O III λ 3760; and (3): TDE-He, which has broad emission feature near He II λ 4686Å but no broad Balmer emission features. More recently, Hammerstein et al. (2023) suggested the fourth spectroscopic class for TDEs, the TDE-featureless, which lacks clear features of the three classes above but can show host galaxy absorption lines.

Besides optical spectroscopic features of optical TDE candidates, several TDEs have been well checked at UV-band: ASASSN-14li (Cenko et al. 2016), iPTF16fnl (Brown et al. 2018), PS16dtm (Blanchard et al. 2017), iPTF15af (Yang et al. 2017), PS1-11af (Chornock et al. 2014), PS18kh (Holoien et al. 2019), AT2018zr (Hung et al. 2019, 2020) and SDSS J014124+010306 (Zhang 2022). Among the reported TDEs, besides the TDE candidate SDSS J014124+010306 reported by Zhang (2022), no one exhibits apparent broad Mg II emission lines. In addition, spectroscopic properties of both broad emission lines and continuum emissions related to central BH accreting process can be applied as apparent signs for broad line AGN (active galactic nucleus), however, those spectroscopic properties can also be expected from assumed central TDEs in host galaxies. Therefore, reporting a central TDE in a definitely normal broad line AGN with pre-existing AGN activity is still a challenge.

Most reported optical TDE candidates are found in quiescent galaxies, partly because identifying TDEs occurring in AGNs is more difficult than in quiescent galaxies due to the intrinsic variability of AGNs, which often exhibit flare-like features (e.g. Elvis et al. 1994; Graham et al. 2017). Furthermore, transients in galaxies with known AGNs have been excluded from TDE search methods (e.g. Hammerstein et al. 2023; van Velzen et al. 2021; Yao et al. 2023) to avoid being overwhelmed by spurious candidates. Several TDE candidates have been reported in AGNs. It has also been suggested that these TDEs may be related to the unique variability of AGNs. Merloni et al. (2015) reported that the changing-look AGN SDSS J015957.64+003310.5 (LaMassa et al. 2015) could be related to a supersolar mass star disrupted by a $10^8 M_{\odot}$ SMBH, leading to the light curve decay being consistent with the $t^{-5/3}$ behavior. This feature is also found in a TDE candidate in Changing-look AGN 1ES 1927+654 (Trakhtenbrot et al. 2019b). Campana et al. (2015) suggested that a flare in low-luminosity AGN IC 3599 could be explained by a repeating partial TDE with a recurrence time of 9.5 years. Blanchard et al. (2017) found that the light curve of a luminous transient PS16dtm in a narrow-line Seyfert 1 galaxy can be fitted with the TDE model. Yan & Xie (2018) analyzed a long-duration TDE expected X-ray flare in the low-luminosity AGN NGC 7213. Shu et al. (2018) proposed that the supersoft X-ray spectrum and the X-ray light curve of AGN GSN 069 can be well explained as a TDE. Liu et al. (2018) reported a candidate TDE in a N-rich quasar SDSS J120414.37+351800.5 via abundance ratio variability. Moreover, Anderson et al. (2020) reported the first radio transient TDE CNSS J001947.3+003527, which is associated with the nucleus of a nearby S0 Seyfert galaxy at 77Mpc. Liu et al. (2020) reported a TDE candidate in SDSS J022700.7-042020.6 by analyzing its light curves. Zhang et al. (2022) proposed that the outburst in an atypical narrow-line Seyfert 1 galaxy CSS J102913+404220 could be explained by a stellar TDE. In addition, Zhang (2022) reported a TDE candidate located in the quasar SDSS J014124+010306 with an apparent broad Mg II emission line.

Among the reported TDE candidates, almost all of them are at low redshift. However, utilizing high-redshift TDEs can provide further information on our understanding of the characteristics and evolution of circumstance of TDEs around central SMBHs in high redshift galaxies and/or AGNs. To date, only four TDEs are at redshift $z > 1$, including Swift J2058.4+0516 at $z \sim 1.185$ in Cenko et al. (2012), J120414.37+351800.5 at $z \sim 2.359$ in Liu et al. (2018), J014124+010306 at $z \sim 1.060$ in Zhang (2022), AT2022cmc at $z \sim 1.193$ in Tanvir et al. (2022). Swift J2058.4+0516 has long-lasting X-ray emission and radio emission (Cenko et al. 2012), SDSS J120414.37+351800.5 at $z \sim 2.359$ is the highest redshift of TDE candidates, which is found in a N-rich quasars (Liu et al. 2018). AT

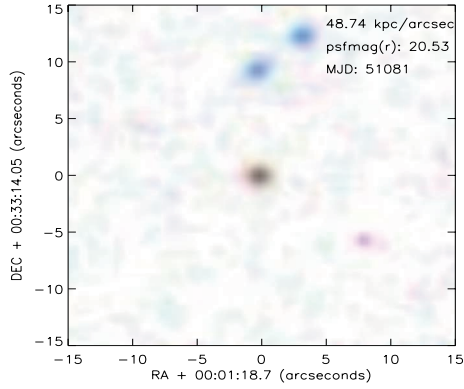


Figure 1. The inverted color image for the SDSS J0001 cut from the SDSS fits image (Flexible Image Transport System), which is constructed through the images of *gri* bands. The kpc/arcsec scale and r band psfmag along with the MJD are shown in the top right region.

2022cmc was suggested as an optically bright and fast relativistic TDE (Andreoni et al. 2022; Pasham et al. 2023; Cikota et al. 2023; Matsumoto & Metzger 2023; Rhodes et al. 2023).

TDEs in AGNs are valuable probes for the central SMBH and the origin of AGN variability. In general, a clear broad Mg II emission line in the spectrum of a TDE candidate indicates that the host galaxy is an AGN. To date, only two events meeting the above criteria have been found. The first one is SDSS J120414.37+351800.5 in Liu et al. (2018), though the quality of the light curve is quite limited, making it difficult to conduct further research. The second one was reported by Zhang (2022), who found a TDE candidate in SDSS J014124+010306 with broad Mg II emission line. Motivated by this, we extensively searched for such candidates within the dataset of SDSS Stripe82 for quasars. We found one candidate in the quasar SDSS J000118.70+003314.0 (=SDSS J0001), characterized by broad Mg II emission lines. This is the highest-redshift optical TDE candidate (~ 1.404) known in AGN. Figure 1 shows a cutout of the image of SDSS J0001.

In this manuscript, we report the long-term photometric SDSS *ugriz*-band variability of SDSS J0001 in Section 2. The theoretical TDE model and fitting procedure are given in Section 3 and Section 4, respectively. We provide our necessary discussion in Section 5. The summary and conclusions are shown in Section 6. Throughout the paper, $H_0=70 \text{ km s}^{-1} \text{ Mpc}^{-1}$, $\Omega_m=0.3$, and $\Omega_\Lambda=0.7$ are adopted.

2 LONG-TERM LIGHT CURVES OF SDSS J0001

Detecting higher redshift TDEs as one of our recent objectives can provide further information on our understanding of the characteristics and evolution of TDEs around central SMBHs in high redshift galaxies and/or AGNs. Visually inspecting the light curves of 7253 high redshift quasars with $z > 1$ in SDSS Stripe8 reported in MacLeod et al. (2010), the light curves provided by the SDSS Stripe82 are checked one by one by eyes, leading to a sample of 20 candidates are obtained. Their light curves have a steep rise phase followed by a smooth decline. Among them, SDSS J0001 has the highest redshift. Therefore, the SDSS J0001 is of interest for our analysis. Detailed discussions on the small sample of TDE candidates in SDSS Stripe82 will be provided in our manuscript currently being prepared.

To construct the long-term variability curves in SDSS *ugriz*-bands of SDSS J0001, we collected optical light curves from the Stripe82

and the PHOTOOBJALL databases. SDSS Stripe82 is a region of the sky near the equator, covering about 300 deg^2 area. It was imaged multiple times by the SDSS in u, g, r, i, and z bands from 2000 to 2008. They are 1.9-2.2 mag deeper than the best SDSS single-epoch data. The more detailed descriptions on the light curves by Stripe82 database¹ (Bramich et al. 2008). The PHOTOOBJALL database², the full photometric catalog quantities for SDSS imaging, contains one entry per detection, with the associated photometric parameters measured by PHOTO, and astrometrically and photometrically calibrated.

First, we collected the public light curves of SDSS J0001 from the Stripe82 database. They had a coverage of 9 years from 1998 September 25 to 2007 October 29 (MJD 51082-54402). Second, the commonly accepted Structured Query Language (SQL) was applied to search for multi-epoch photometric light curves of SDSS J0001 in the PHOTOOBJALL database from data release 16 (DR16, Blanton et al. (2017); Ahumada et al. (2020)), with the corresponding SQL query shown in the Appendix A. In this manuscript, only the data points are considered with magnitudes greater than 10 and less than 25 and positive uncertainties smaller than tenth of the corresponding magnitudes. Meanwhile, we compiled the *ugriz*-band light curves from the PHOTOOBJALL, using the SDSS point-spread function (PSF) magnitudes because SDSS J0001 is a point-like source. The first five panels of Figure 2 display the light curves in the *ugriz*-band. In each panel, solid blue and green circles plus error bars represent the data points and the corresponding 1σ uncertainties from the Stripe82 and the PHOTOOBJALL databases, respectively. The light curves with ~ 60 data points in each band have the corresponding meantime step about 55 days.

The light curves of SDSS J0001 exhibit a clear rise-to-peak followed by a smooth decline trend, this unique variability is different from the continuous and long-term variability of EVQs (extreme variability quasars) (Rumbaugh et al. 2018; Ren et al. 2024), resembling the variability behavior of common broad line AGN but with larger variability amplitudes. In other words, we don't exclude the possibility that SDSS J0001 is an EVQ, but we expect a TDE to explain the unique variability in the light curve.

To further analyze the characteristics of the light curves of SDSS J0001, we also characterized the light curves by applying other phenomenological models. Following van Velzen et al. (2021), we modeled the light curves with a Gaussian rise and an exponential decay. The fitting results to the *g*-band light curve of SDSS J0001 are shown in the left panel of Figure 3, with fitting parameters $\log(\sigma)=2.99^{+0.20}_{-0.14}$ days and $\log(\tau)=3.46^{+0.29}_{-1.19}$ days, respectively. The corresponding errors are the 1σ uncertainties determined by the Least Squares Method. The parameters $\log(\sigma)$ and $\log(\tau)$ of SDSS J0001, due to the longer duration of light curve, undoubtedly exceed those reported in van Velzen et al. (2021) for TDEs. However, the $\sigma/\tau \sim 0.86$ remains within their reported range (0.04-0.90). Following van Velzen et al. (2021), the peak bolometric luminosity, photosphere temperature and radius are $L = 2.28^{+0.66}_{-0.51} \times 10^{45} \text{ erg/s}$, $T = 2.64^{+0.04}_{-0.05} \times 10^4 \text{ K}$, $R = 2.56^{+0.33}_{-0.39} \times 10^{15} \text{ cm}$, respectively. Compared to the TDE candidates reported in Mockler et al. (2019); van Velzen et al. (2021); Hammerstein et al. (2023), the L , R , T of SDSS J0001 are moderate among these TDE candidates.

Additionally, following Graham et al. (2017), we further characterized the SDSS J0001 flare based on shape parameters utilizing the Weibull distribution. The Weibull shape parameter to the *g*-band light

¹ https://das.sdss.org/va/strip82_variability/SDSS_82_public

² <https://skyserver.sdss.org/dr16/en/help/browser/browser.aspx#&hist>

curve of SDSS J0001 is represented by $\log(a)=0.016^{+0.002}_{-0.001}$, and the scale parameter is denoted by $\log(s)=0.016^{+0.02}_{-0.02}$, respectively. The fitting results are shown in right panel of Figure 3. Notably, the parameter $\log(a)$ and $\log(s)$ of SDSS J0001 deviate completely from the parameter distribution of simulated flares according to single-point single-lens model (1S1L) and lensing candidates (see details in Fig 15 of [Graham et al. \(2017\)](#)). A small value of "a" indicates low symmetry, consistent with the flare characteristics of TDE. Additionally, the g-r color evolutions of SDSS J0001 (as shown in the bottom right panel of Figure 2) closely resemble the evolutionary characteristics of TDEs described in [Yao et al. \(2023\)](#).

3 THEORETICAL TDE MODEL

Based on the discussions above, the theoretical TDE model can be considered to describe the long-term variability of SDSS J0001 shown in the first five panels of Figure 2. The details of the theoretical TDE model please refer to [Guillochon & Ramirez-Ruiz \(2013\)](#), [Guillochon et al. \(2014, 2018\)](#), and [Mockler et al. \(2019\)](#). We briefly describe the model below.

3.1 Dynamic Model

Assuming a TDE occurs when a star with mass M_* is tidally disrupted by an SMBH with a mass of M_{BH} , the template of fallback material rate \dot{M}_{fbt} evolves as

$$\dot{M}_{\text{fbt}} = \frac{dM}{dE} \frac{dE}{dt} \sim \frac{(2\pi G M_{\text{BH}})^{2/3} dM}{3 t^{5/3} dE}, \quad (1)$$

where dM represents the debris mass, dE is the specific binding energy after a star is torn apart, and G is the gravitational constant, dM/dE as distribution of debris mass on binding energy can be provided by TDEFIT/MOSFIT based on hydrodynamical simulations in [Guillochon et al. \(2014, 2017, 2018\)](#). Considering the viscous delay effects discussed in [Guillochon & Ramirez-Ruiz \(2013\)](#); [Mockler et al. \(2019\)](#), the viscous-delayed accretion rates \dot{M}_a from the fallback material rate \dot{M}_{fbt} are given by

$$\dot{M}_a(T_v, \beta) = \frac{\exp(-t/T_v)}{T_v} \int_0^t \exp(t'/T_v) \dot{M}_{\text{fbt}} dt', \quad (2)$$

where T_v is the viscous time. [Guillochon et al. \(2014, 2018\)](#) and [Mockler et al. \(2019\)](#) developed the TDEFIT/MOSFIT code through hydrodynamical simulations for a standard TDE case with a star with mass of $M_* = 1M_\odot$ disrupted by a SMBH with mass of $M_{\text{BH},6} = 1$, where $M_{\text{BH},6}$ represents central BH mass in units of $10^6 M_\odot$. The code presents the dM/dE values by varying the impact parameter β^{temp} for different values, and considering a polytropic index of $\gamma = 4/3$ or $\gamma = 5/3$.

The numerical results then can be taken as a template for deriving the $\dot{M}_a(T_v, \beta)$ with β different from β^{temp} through interpolations. We collect the dM/dE values from the TDEFIT/MOSFIT code by varying the impact parameters value β^{temp} from 0.6 to 4.0 for the scenario of $\gamma = 4/3$ (23 values) or from 0.5 to 2.5 for $\gamma = 5/3$ (20 values) and linear varying $\log T_v^{\text{temp}}$ from -3 to 0 (31 values). Hence, we construct templates of the time-dependent viscous-delayed accretion rates \dot{M}_a^{temp} of 713 (620) viscous-delayed accretion rates for polytropic index $\gamma = 4/3$ (or $\gamma = 5/3$). Figure 4 illustrate temporal evolution of \dot{M}_{fbt} and \dot{M}_a for some sets of $\{T_v, \beta\}$ as marked in the figure. One can observe that \dot{M}_a as a function of time peaks at a later time and has a lower peak value than that of \dot{M}_{fbt} . This is reasonable regarding the mass reservation of the central accretion disk.

We calculate the viscous-delayed accretion rate $\dot{M}_a(T_v, \beta)$ for a given set of $\{T_v, \beta\}$ through linear interpolations. The first linear interpolations are applied to obtain the viscous-delayed accretion rates for the input T_v using the following two equations

$$\dot{M}_a(T_v, \beta_1^{\text{temp}}) = \dot{M}_a^{\text{temp}}(T_{v1}^{\text{temp}}, \beta_1^{\text{temp}}) + \frac{T_v - T_{v1}^{\text{temp}}}{T_{v2}^{\text{temp}} - T_{v1}^{\text{temp}}} [\dot{M}_a^{\text{temp}}(T_{v2}^{\text{temp}}, \beta_1^{\text{temp}}) - \dot{M}_a^{\text{temp}}(T_{v1}^{\text{temp}}, \beta_1^{\text{temp}})], \quad (3)$$

$$\dot{M}_a(T_v, \beta_2^{\text{temp}}) = \dot{M}_a^{\text{temp}}(T_{v1}^{\text{temp}}, \beta_2^{\text{temp}}) + \frac{T_v - T_{v1}^{\text{temp}}}{T_{v2}^{\text{temp}} - T_{v1}^{\text{temp}}} [\dot{M}_a^{\text{temp}}(T_{v2}^{\text{temp}}, \beta_2^{\text{temp}}) - \dot{M}_a^{\text{temp}}(T_{v1}^{\text{temp}}, \beta_2^{\text{temp}})],$$

where $\beta_1^{\text{temp}}(T_{v1}^{\text{temp}})$ and $\beta_2^{\text{temp}}(T_{v2}^{\text{temp}})$ are two adjacent template $\beta(T_v^{\text{temp}})$ values that satisfy $\beta_1^{\text{temp}} \leq \beta \leq \beta_2^{\text{temp}}$ ($T_{v1}^{\text{temp}} \leq T_v \leq T_{v2}^{\text{temp}}$). Then the viscous-delayed accretion rates for the input T_v and β can be obtained by

$$\dot{M}_a(T_v, \beta) = \dot{M}_a(T_v, \beta_1^{\text{temp}}) + \frac{\beta - \beta_1^{\text{temp}}}{\beta_2^{\text{temp}} - \beta_1^{\text{temp}}} [\dot{M}_a(T_v, \beta_2^{\text{temp}}) - \dot{M}_a(T_v, \beta_1^{\text{temp}})]. \quad (4)$$

We show an example in Figure B1 of results through these three linear interpolation processes in the Appendix B.

For a general TDE with BH mass M_{BH} and star mass M_* in units of M_\odot , we calculate the values of \dot{M} as a function of time by adopting the following scaling relations ([Mockler et al. 2019](#)),

$$\dot{M} = M_{\text{BH},6}^{-0.5} \times M_*^2 \times R_*^{-1.5} \times \dot{M}_a(T_v, \beta) \quad (5)$$

$$t = (1+z) \times M_{\text{BH},6}^{0.5} \times M_*^{-1} \times R_*^{1.5} \times t_a(T_v, \beta),$$

where R_* represents the stellar radius in units of R_\odot and z is the redshift of the host galaxy of the TDE. Additionally, we adopt the known mass-radius relation for main sequence stars in [Tout et al. \(1996\)](#).

3.2 Radiation Model

The radiating region is assumed to be a standard blackbody photosphere, as discussed in [Mockler et al. \(2019\)](#). The time-dependent effective blackbody temperature $T_p(t)$ is estimated with

$$T_p(t) = \left(\frac{L}{4\pi\sigma_{\text{SB}}R_p^2} \right)^{1/4} = \left[\frac{\eta\dot{M}(t)c^2}{4\pi\sigma_{\text{SB}}R_p^2} \right]^{1/4}, \quad (6)$$

where L is the time-dependent bolometric luminosity given by $L = \eta\dot{M}(t)c^2$, η represents the energy transfer efficiency that is lower than 0.4 ([Guillochon et al. 2014](#); [Mockler et al. 2019](#)), σ_{SB} is the Stefan-Boltzmann constant, c is the speed of light, and $R_p(t)$ is the radius of the photosphere. $R_p(t)$ ranges from the minimum R_{isco} (event horizon radius) to the maximum semimajor axis (a_p) of the accreting mass, it is assumed to be a power-law dependence on L (e.g. [Mockler et al. 2019](#)), i.e.

$$R_p(t) = R_0 \times a_p (L/L_{\text{Edd}})^{l_p} = R_0 \times a_p \left[\frac{\eta\dot{M}(t)c^2}{1.3 \times 10^{38} M_{\text{BH}}} \right]^{l_p}, \quad (7)$$

where L_{Edd} represents the Eddington luminosity ($L_{\text{Edd}} \equiv 4GM_{\text{BH}}c/\kappa$ and κ is the mean opacity to Thomson scattering assuming solar metallicity), R_0 is a dimensionless free parameter, l_p

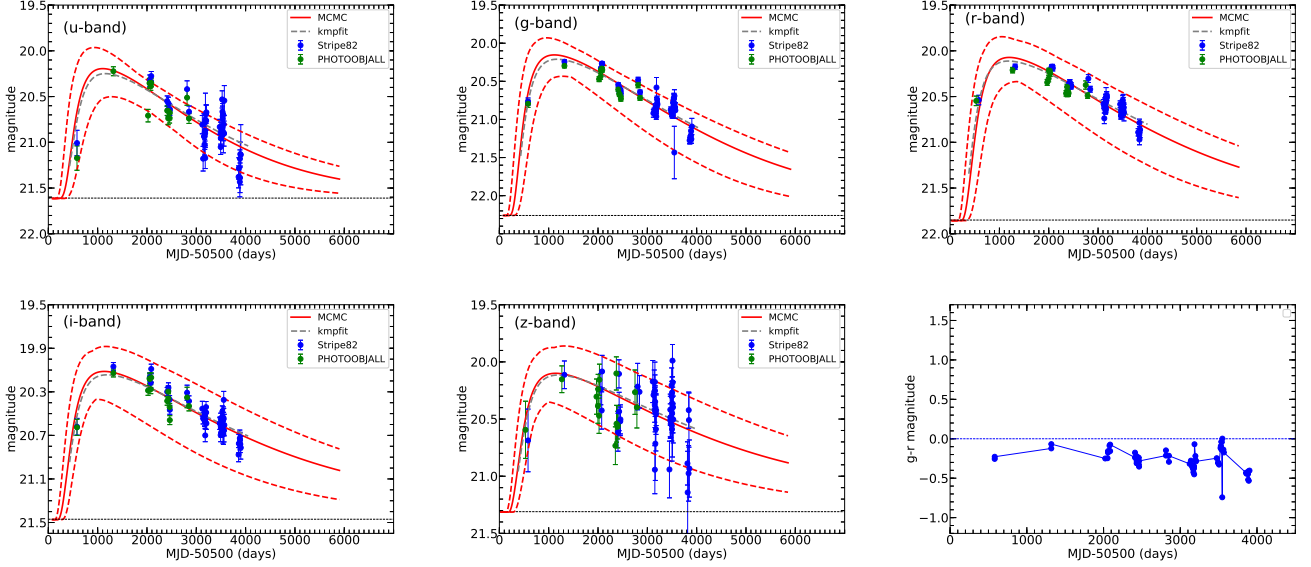


Figure 2. Top panels and bottom left two panels show the observed *ugriz* band light curves of SDSS J0001 and the best fit with the TDE model. Data points from both the Stripe82 and the PHOTOOBJALL databases have been used in our analysis. In each panel, solid blue and green circles with error bars represent the data points and the corresponding 1σ uncertainties from the Stripe82 and the PHOTOOBJALL databases, respectively. The grey dashed lines represent the fitting result by the *kmpfit* method. The red solid and dashed red lines show the best fit and the corresponding confidence bands determined by the 1σ uncertainties of the model parameters with the MCMC technique, which is described and discussed in detail in Section 4. The black dotted line represents the contributions from the host galaxy. Bottom right panel shows the color (*g-r*) evolution of SDSS J0001.

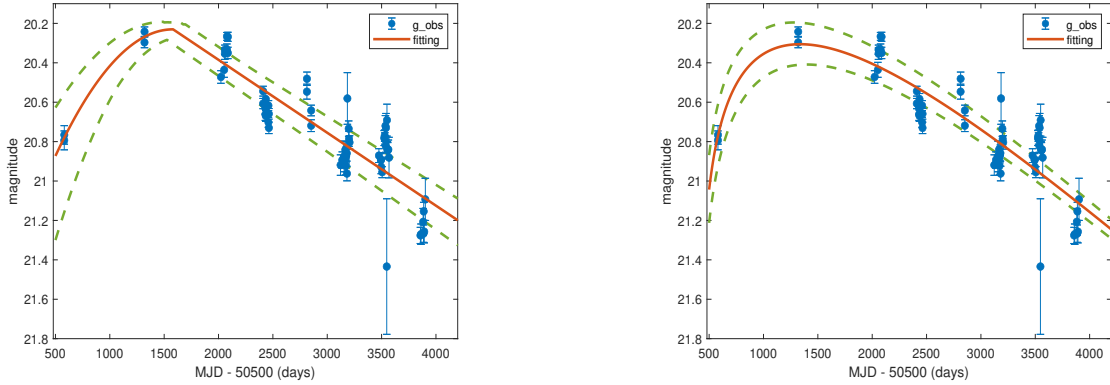


Figure 3. Best fit (black solid line) to the SDSS *g*-band light curve of SDSS J0001 (solid blue circles), with a Gaussian rise and an exponential decay (left panel) and Weibull distribution (right panel). The red solid and dashed green lines show the best fit and the corresponding confidence bands determined by the 1σ uncertainties of the model parameters with the Least Squares Method, respectively.

represents the power-law exponent and t_p is time of the peak accretion rate. The value of a_p is given by

$$a_p = \left[GM_{\text{BH}} \times \left(\frac{t_p}{2\pi} \right)^2 \right]^{1/3}. \quad (8)$$

The time-dependent emission spectrum in the rest frame can be calculated as

$$F_\lambda(t) = \frac{2\pi hc^2}{\lambda^5} \frac{1}{e^{hc/(k\lambda T_p(t))} - 1} \left[\frac{R_p(t)}{D(z)} \right]^2, \quad (9)$$

where $D(z)$ is the luminosity distance at redshift z .

After calculating the time-dependent $F_\lambda(t)$ in the observer frame and then convolved with the transmission curves of the SDSS *ugriz* filters, the time-dependent apparent magnitudes $mag_{u,g,r,i,z}(t)$ can be determined in the corresponding SDSS bands. Then, we can

check whether the MOSFIT TDE model can be applied to describe the long-term variability of SDSS J0001 shown in the first five panels of Figure 2.

4 FITTING PROCEDURE AND RESULTS

We fit the light curves in the *ugriz* bands of SDSS J0001 by the MOSFIT TDE model. The free parameters of the model include M_{BH} , M_* , R_* , β , T_v , η , R_0 , and l_p . The brightness [*mag*₀(*u, g, r, i, z*)] of the host galaxy is taken as free parameter. The model requires that the tidal disruption radius R_{TDE} derived from a set of model parameters is larger than the event horizon of the central BH. In order to fit the observed light curves, the following two steps are applied. First, we fit the light curves with the Levenberg-Marquardt least-squares optimization technique (the *kmpfit* module in PYTHON;

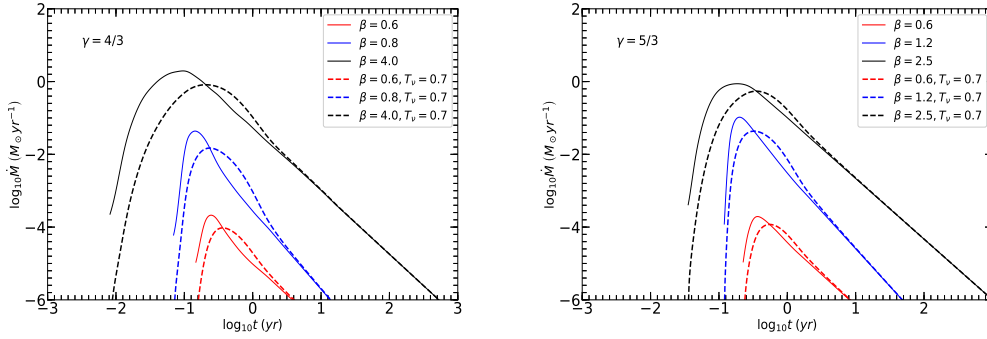


Figure 4. The fallback material rate (\dot{M}_{fbr}) (solid lines) and viscous-delayed accretion rate (\dot{M}_{at} with $T_v = 0.7$ as an example) (dashed lines) of a $1M_{\odot}$ star disrupted by $10^6 M_{\odot}$ black hole determined through the theoretical TDE model with polytropic index $\gamma = 4/3$ (left panel) and $\gamma = 5/3$ (right panel), respectively. As shown in the legend in each panel, line styles in different colors represent the results with different β .

Markwardt 2009). Being due to the poorly light curve sampling, the uncertainties of the model parameter cannot be constrained with the kmpfit module. Thus, we secondly adopt the Markov Chain Monte Carlo (MCMC) technique (the emcee package in PYTHON) (Foreman-Mackey et al. 2013) to improve our fit. The prior model distributions, listed in Table 1, are set based on the results of the kmpfit module. 400 MCMC iterations with 500 walkers have been applied in our MCMC fit.

Our fitting results are shown in the first five panels of Figure 2. The derived posterior distributions of the model parameters are shown in Figure 5, and best fit parameters are reported in Table 1. The reduced χ^2/dof of our fit is ~ 4.5 . One can observe that the light curves of SDSS J0001 can be explained as a tidal disruption of a main sequence star with mass of $1.905^{+0.023}_{-0.009} M_{\odot}$ by a SMBH with mass of $M_{\text{BH}} \sim 6.5^{+3.5}_{-2.6} \times 10^7 M_{\odot}$. The predicted peak brightness of the TDE event is at $1.83^{+0.46}_{-0.33}$ years. The total energy of the event derived from our fit is 2.38×10^{53} ergs and about $0.78 M_{\odot}$ of debris mass is accreted by the central SMBH (corresponding $1.12 M_{\odot}$ of the disrupted star are ejected).

The model predicted time-dependent bolometric luminosity and photosphere temperature of SDSS J0001 are shown in Figure 6. The peak bolometric luminosity and photosphere temperature are $1.18^{+0.26}_{-0.31} \times 10^{45}$ erg/s and $2.30^{+0.30}_{-0.28} \times 10^4$ K, respectively. Adopting the parameters of four TDEs reported by Mockler et al. (2019), we also compare the time-dependent bolometric luminosity and photosphere temperature of the four TDEs with SDSS J0001 in Figure 6. Among them the TDEs of D1-9 (Gezari et al. 2008) and D3-13 (Gezari et al. 2008) have a relatively high bolometric luminosity, and TDEs ASASSN-14ae (Holoien et al. 2014; Brown et al. 2016) and iPTF-axa (Hung et al. 2017) have relatively a low bolometric luminosity. It is found that the intrinsic peak bolometric luminosity and photosphere temperature of SDSS J0001 are moderate among these TDE candidates.

5 DISCUSSIONS

5.1 Timescale of the TDE Candidate SDSS J0001

We collected light curves of the typical TDE candidates in Mockler et al. (2019) and re-described them using their model pa-

Table 1. Parameters of the TDE model derived from our Kmpfit and MCMC fit to the light curves of SDSS J0001.

Parameters	Prior distribution	Kmpfit	MCMC fit
$\log(M_{\text{BH}}, \text{e})$	[-1, 3]	1.79	1.81 $^{+0.19}_{-0.22}$
$\log(M_{\star}/M_{\odot})$	[-2, 1.7]	0.28	0.28 $^{+0.005}_{-0.007}$
$\log(\beta)$ (4/3)	[-0.22, 0.6]	0.25	0.25 $^{+0.084}_{-0.063}$
$\log(T_v)$	[-3, 0]	-0.76	-0.84 $^{+0.21}_{-0.24}$
$\log(\eta)$	[-3, -0.4]	-0.97	-0.98 $^{+0.15}_{-0.13}$
$\log(R_0)$	[-3, 3]	-0.82	-0.77 $^{+0.22}_{-0.23}$
$\log(l_p)$	[-3, 0.6]	-0.82	-0.82 $^{+0.34}_{-0.13}$
$mag_0(u)$	[20, 30]	21.56	21.61 $^{+0.72}_{-0.56}$
$mag_0(g)$	[20, 30]	22.26	22.25 $^{+0.49}_{-0.53}$
$mag_0(r)$	[20, 30]	21.80	21.85 $^{+0.60}_{-0.43}$
$mag_0(i)$	[20, 30]	21.50	21.47 $^{+0.62}_{-0.35}$
$mag_0(z)$	[20, 30]	21.31	21.31 $^{+0.57}_{-0.59}$

rameters, as applied in our method, as shown in Figure 7³. Compared with these TDEs, SDSS J0001 has the longest timescale. Noting that $t \propto M_{\text{BH}}^{1/2} M_{\star}^{-1} R_{\star}^{1.5}$ and considering the mass-radius relation for main sequence stars, we have $t \propto M_{\text{BH}}^{1/2} M_{\star}^{1/2}$. The long timescale is partially due to the large black hole mass and large stellar mass. More important, as shown in Figure 4 (see also Fig 5 of Guillochon & Ramirez-Ruiz (2013)), the timescale is sensitive to the impact parameter β . A larger β leads to a longer timescale. The derived β value for SDSS J0001 is 1.77, which is indeed much larger than other TDE candidates reported by Mockler et al. (2019) except for D3-13. The β value of TDE D3-13 is 1.8. Its timescale exceeds one thousand days. Considering the M_{BH} of SDSS J0001 and the time dilation effect of SDSS J0001 at high redshift ($z = 1.4$), its intrinsic timescale is comparable to TDE D3-13.

Trakhtenbrot et al. (2019a) proposed that the slowly-decayed UV-optical transient AT 2017bgt is likely a new type of flare associated with accreting SMBHs, and suggested that it is unlikely to be a TDE driven flare. Inspecting the light curves of AT 2017bgt in the optical, UV, and X-ray bands reported by Trakhtenbrot et al. (2019a), the rise-to-peak and followed by smooth declining trend in UV band light curve is apparent and can be well expected by a central TDE.

³ We collected the light curves of the 13 TDE candidates from <https://tde.space/>.

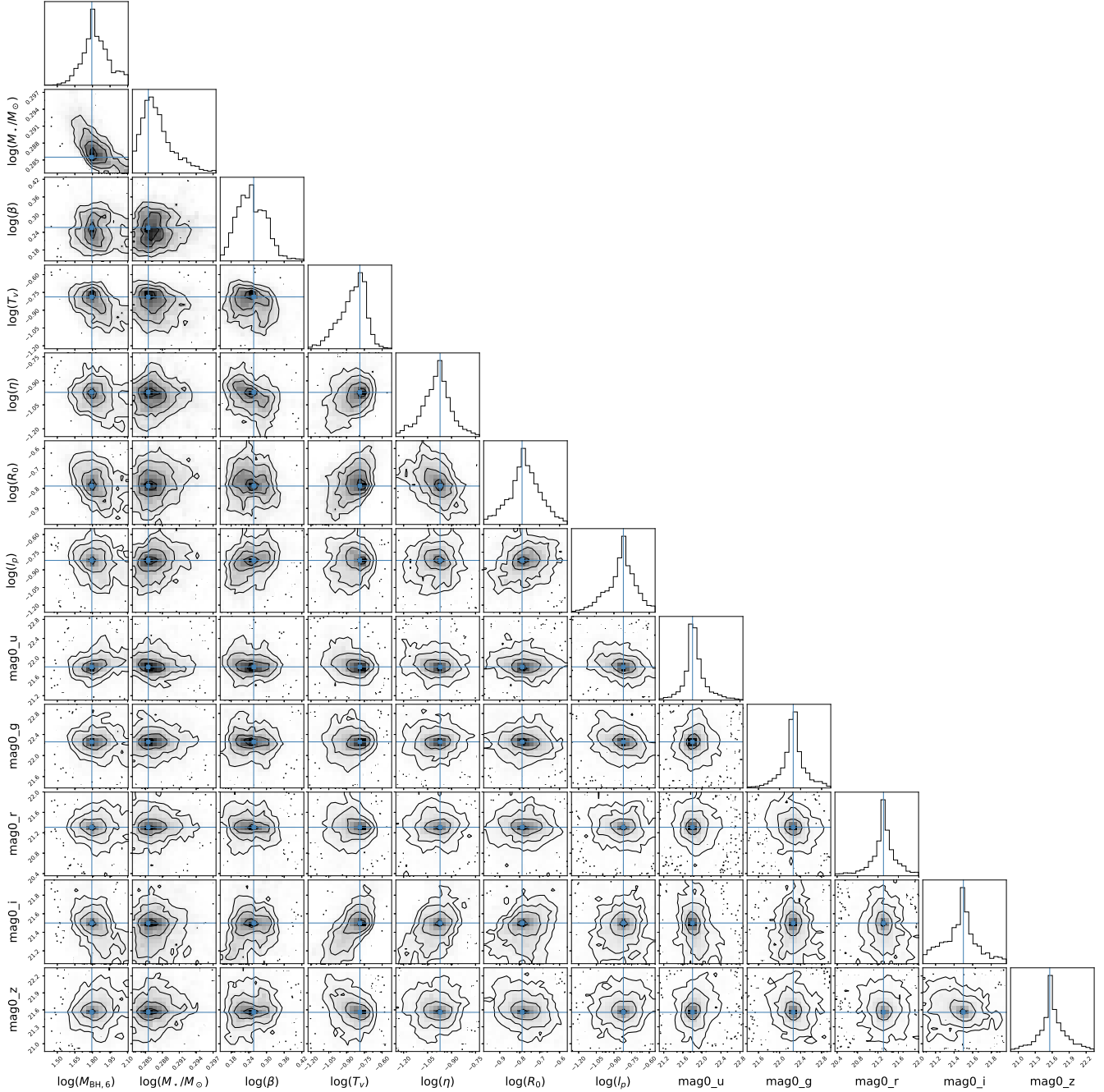


Figure 5. Corner plot shows the posterior probability distributions of the TDE model parameters obtained from the MCMC technique. In each panel, the three circles from outer to inner represent 3σ , 2σ , and 1σ confidence levels, and the blue dot in the center of each contour marks the position of the best-fit parameter.

We compare it with other TDE candidates reported by [Mockler et al. \(2019\)](#) in Figure 7. We also present the theoretical light curves with our TDE model code by adopting the parameters the same as that reported by [Mockler et al. \(2019\)](#). Using the `kmpfit` module, we fit its UVW1 and UVW2 light curves, with the UVW2 fitting curve is also shown in Figure 7. Our findings suggest that these curves are well represented by the TDE model with parameters of $M_* = 7.76M_\odot$,

$M_{\text{BH}} = 2.0 \times 10^6 M_\odot$, $\beta = 1.14$, and $\gamma = 4/3$. We cannot entirely rule out the possibility that AT 2017bgt is a TDE candidate.⁴

5.2 Host galaxy and SMBH mass

The SDSS spectrum of SDSS J0001 (plate-mjd-fiberid = 1091-52902-525) observed around the epoch of peak brightness of its

⁴ We should carefully note that the loss of data points around 200-350 days of AT2017bgt light curve makes uncertainty of the late decaying behavior of AT 2017bgt.

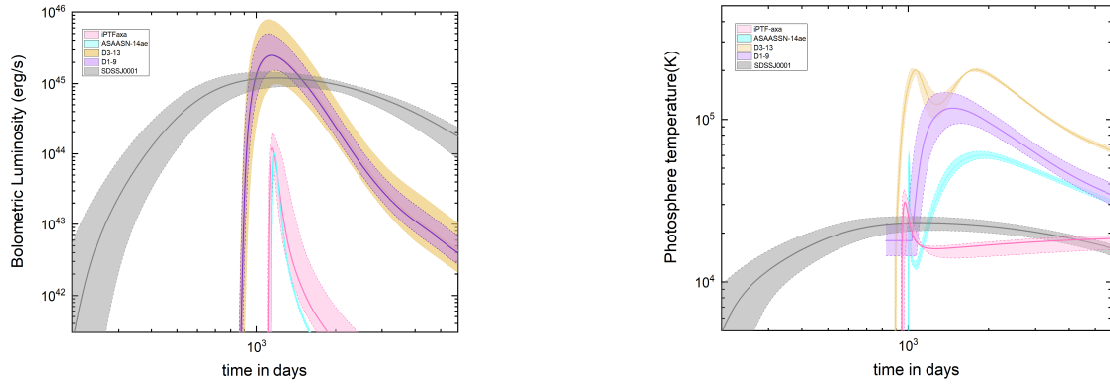


Figure 6. Temporal Evolution of the bolometric luminosity (*left panel*) and photosphere temperature (*right panel*) of SDSS J0001 in comparison with that of four events from [Mockler et al. \(2019\)](#) as marked in each panel with different colors. All events align with their peak bolometric luminosity or photosphere temperature, and the time is in the observer’s frame. The shaded regions indicate the confidence bands determined by uncertainties of model parameters.

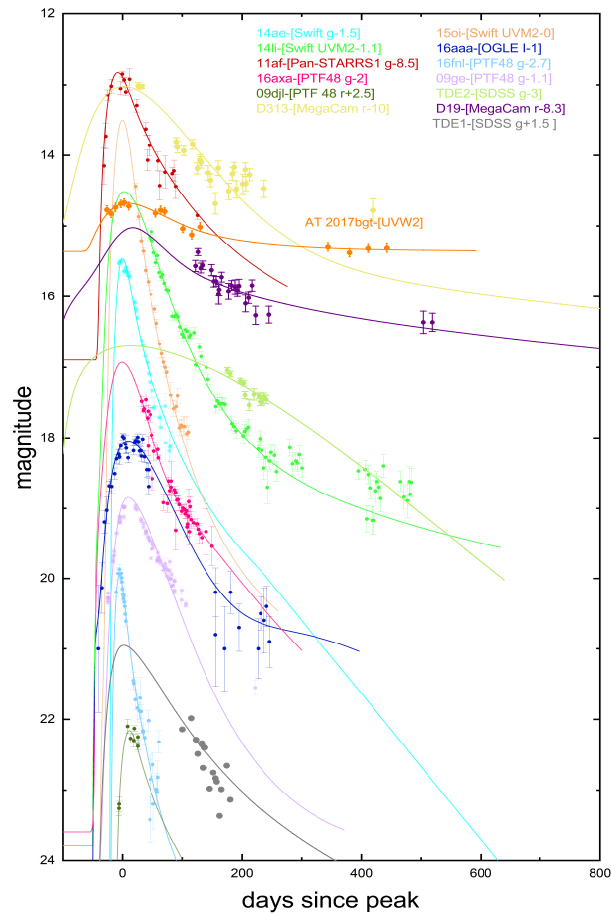


Figure 7. Comparison of the slowly-decayed UV-optical transient AT 2017bgt reported by [Trakhtenbrot et al. \(2019a\)](#) with the 13 TDE candidates reported by [Mockler et al. \(2019\)](#). The best fit results by applying the fitting parameters from [Mockler et al. \(2019\)](#) in our fitting procedure. Note that no theoretical light curve is available for the TDE candidate PS1-10jh because the estimated tidal disruption radius is smaller than the event horizon of the central BH.

light curve, collected from SDSS DR16 ([Ahumada et al. 2020](#)), is shown in Figure 8. It has a quasar-like spectrum with apparent broad Mg II emission line. [Shen et al. \(2011\)](#) estimated its virial BH mass as $4.9 \times 10^8 M_{\odot}$ through broad Mg II emission lines, which is approximately 7.5 times larger than that derived from our analysis. It is possible that the broad Mg II emission materials in SDSS J0001 include contributions from TDE debris near the central BH. Similar as

what have been discussed in [Zhang et al. \(2019\)](#); [Zhang \(2021, 2022\)](#) for broad emission line regions (BLRs) if tightly associated with TDEs debris, non-virial dynamic properties of broad emission line clouds related to TDE debris could be expected, such as the results in the TDE candidate ASASSN-14li in [Holoien et al. \(2016\)](#): stronger emissions leading to wider line widths of broad H_{α} which are against the results by the virialization assumptions to BLRs clouds. The non-

virial dynamic properties of broad line clouds nearer to central BH in SDSS J0001 could be applied to explain the TDE model determined BH mass smaller than the virial BH mass.

In addition to the virial black hole mass and the black hole mass determined by the MOSFIT model, we also tried to estimate the black hole mass using *TDEmass* (Ryu et al. 2020), which calculates the masses of the black hole and the disrupted star based on the peak luminosity and temperature of the flare. Using input parameters obtained from a Gaussian rise and an exponential decay model. We found that *TDEmass* was unable to determine the black hole mass and the disrupted star mass for SDSS J0001, as the peak luminosity and temperature fall outside the limits explored by the *TDEmass*, similar to the four TDE candidates with high luminosities above 10^{45} erg/s reported by Hammerstein et al. (2023).

5.3 Probability of the long-term variability of SDSS J0001 as intrinsic AGN variability

Moreover, As we all know, SMBHs are common in broad line AGN, and star formations could be commonly expected around accretion flows as well discussed in Dittmann & Miller (2020); Krumholz et al. (2009). Therefore, TDE candidates could be expected in broad-line AGN. The results mentioned above are derived from an assumption that the long-term variability of SDSS J0001 are related to a central TDE. Thus, it is necessary to evaluate the possibility that the long-term variability of SDSS J0001 results from intrinsic AGN activity. The intrinsic AGN flares can be described by the damped random walk (DRW) process (also known as the Ornstein–Uhlenbeck process or the Gaussian first-order continuous autoregressive (CAR) process (e.g. Kelly et al. 2009; Zu et al. 2013; Kozłowski et al. 2010; Zu et al. 2016). Many studies have investigated AGN variability properties through the DRW/CAR process, such as the results well discussed in MacLeod et al. (2010, 2012); Andrae et al. (2013); Zhang et al. (2021); Sheng et al. (2022). The DRW/CAR process (or stochastic processes) with damping timescale τ (a timescale for the time series to become uncorrelated) and intrinsic variability amplitude σ ($SF_\infty \sim \sigma\sqrt{\tau}$ as the parameter used in MacLeod et al. (2010)). To describe the stochastic variability of AGN light curves, the public code JAVELIN⁵ has been widely applied.

Then, based on the public JAVELIN code, the left panel of Figure 9 shows the best fit and the corresponding 1σ confidence band to the photometric SDSS g -band light curve with the JAVELIN code. The reduced χ^2 of the fit is $\chi^2/dof \sim 0.98$. The right panel of Figure 9 shows the posterior distributions of the DRW process parameters determined through the MCMC fit. We have $\ln(\tau/\text{days}) \sim 6.15^{+0.44}_{-0.48}$ ($\tau \sim 470^{+260}_{-178}$ days) and $\ln(\sigma/(\text{mag}/\text{days}^{0.5})) \sim -1.38^{+0.17}_{-0.18}$.

Before proceeding further, it is necessary to test if the DRW/CAR model could be applied to the light curve length of the SDSS J0001. Following MacLeod et al. (2010), we calculate the $\Delta L_\infty \equiv \ln(L_{best}/L_\infty)$, where L_{best} is the likelihood of the stochastic model, L_∞ is the likelihood that $\tau \rightarrow \infty$, indicating that the light curve length is too short to accurately measure τ . We calculate the $\Delta L_\infty = 0.99$ for the g -band light curve of SDSS J0001. This means that the time duration of the light curve is long enough (MacLeod et al. (2010) exclude cases where $\Delta L_\infty \leq 0.05$) for accurately measuring the process parameters. On the other hand, based on the discussions in Kozłowski (2017) regarding the input DRW timescale (τ_{inp}) and experiment length (t_{exp}), we calculate $\rho_{inp} \sim 0.1$ (here, $\rho_{inp} = \tau_{inp} \times t_{exp}^{-1}$), indicating that intrinsic process parameters can be recovered through

applications of CAR/DRW process to describe the long-term variability of SDSS J0001.

Based on the determined process parameter τ , through the CAR process discussed in Kelly et al. (2009), mock light curves $X(t)$ to trace intrinsic AGN activity can be created by

$$dX(t) = -\frac{1}{\tau}X(t) + \sigma_*\sqrt{dt}\epsilon(t) + bdt, \quad (10)$$

where $\epsilon(t)$ represents a white noise process with zero mean and a variance of 1 (created by *randomn* function in IDL in this analysis), bdt is the mean magnitude of the light curve. For a given light curve, the relation between CAR process parameter τ , σ_* , and variance of the light curve (ν) can be estimated as $\nu \sim \tau\sigma_*^2/2$. Here, the used parameter σ_* in the CAR process above has similar physical meanings as σ applied in JAVELIN code, but σ_* and σ are not exactly equal.

We use the CAR process model to generate mock g -band light curves by adopting $bdt = 20.76$ (the mean magnitude of g -band light curve of SDSS J0001) and $\nu = 0.07$ (the variance of g -band light curve of SDSS J0001). The CAR process parameter τ is randomly selected from 470-178 to 470+260 (determined τ plus/minus uncertainties for SDSS J0001) and the parameter σ_* is determined by $\nu \sim 0.07$. The mock light curves are sampled the same as the data points. The uncertainties of $F_{sim}(t)$ of the mock data are simply determined as the relative error of the observational data,

$$\delta F_{sim}(t) = F_{sim}(t) \times \frac{\delta F_{obs}(t)}{F_{obs}(t)}, \quad (11)$$

where F_{obs} and δF_{obs} as the observational flux of g -band light curve and the corresponding uncertainty of SDSS J0001. Based on Equations (10) and (11), we generated 10^5 mock light curves and fitted them with the TDE model. Since the best fit with the TDE model to the observational data of SDSS J0001 is 4.5, we selected a TDE candidate with the criterion of $\chi^2/dof < 4.5$. This means that the TDE model fit to the selected mock light curve is comparable to that for SDSS J0001. Finally, we found 9 light curves that can be well described by the theoretical TDE model. Therefore, the probability is about 0.009%. Figure 10 displays mock light curves that pass and do not pass the criterion for evaluating whether the light curves can fit with the TDE model.

Note that simulations by Zhang (2022) were made by setting the uniform distribution of $\tau \in \{50, 5000\}$ days (similar to reported values of quasars in Kelly et al. (2009); MacLeod et al. (2010)) but calculating the σ_* using the variance of the light curve of SDSS J0141. The logic of this approach is to estimate the probability that a light curve with $\tau \in \{50, 5000\}$ days for normal quasars can be modeled with the TDE model. Following this approach, we calculate the upper limit of the probability $p = 0.144\%$ for SDSS J0001 by adopting $\tau \in \{50, 5000\}$ days in a normal distribution and using $\tau\sigma_*^2/2 \sim 0.07$. In this work, we estimate the probability based on the DRW model-determined parameters and their uncertainties ($\tau \sim 470^{+260}_{-178}$) and then calculate the probability. The logic of this approach is that, if the observational data are from the variability of SDSS J0001, what is the chance probability of the data being fitted with the TDE model by considering the observational uncertainty? The derived probability is 0.009%.

Based on the discussions above, there are further clues to support the potential central TDE in SDSS J0001. Moreover, Zhang (2023) proposed a method to search for probable hidden TDEs in normal broad line AGN with apparent intrinsic variability by considering the effects of contributions of TDEs expected variability to normal AGN variability. TDE candidates could be widely expected in broad-line AGN even with stronger activities. In other words, before

⁵ <https://github.com/nye17/javelin#citation>

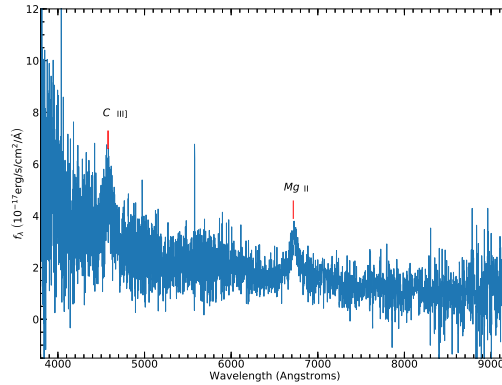


Figure 8. Optical spectrum of SDSS J0001 in observer frame. The vertical solid red lines mark positions of the broad lines.

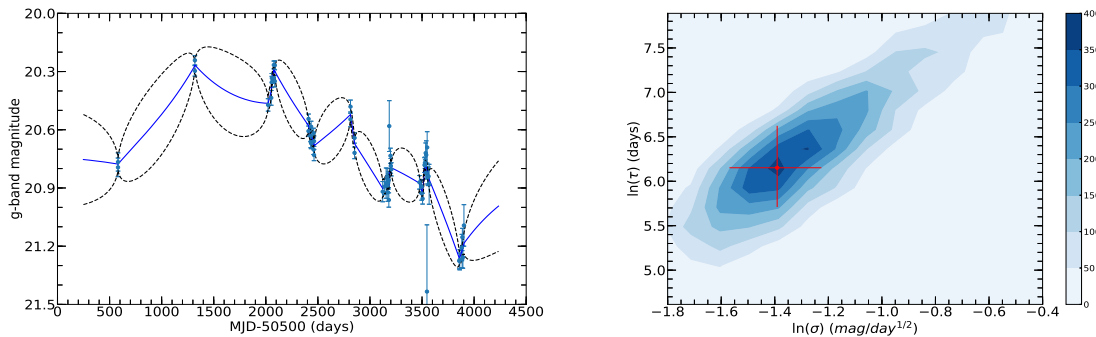


Figure 9. *Left panel*—The best fit with the JAVELIN code (solid blue line) and the corresponding 1σ confidence band (the black dashed lines) to the g -band light curve of SDSS J0001 in observer frame. *Right panel*— Two-dimensional posterior distributions in the $\tau - \sigma$ plane derived from the MCMC fit, where the red circle with error bar indicate the central values and 1σ uncertainties of $\ln(\tau)$ and $\ln(\sigma)$.

detecting and reporting hidden TDEs in normal broad-line AGN with apparent variability, preliminary clues can be provided to study the connections between intrinsic AGN activity and variability related to TDEs. This can be achieved by detecting and reporting more TDE candidates in broad-line AGN (quasars) without apparent long-term variability outside of the time durations of expected TDEs. This is our main objective in the current stage.

5.4 Alternative explanations for the flare observed in SDSS J0001

Other possibilities may also explain the flare shown in the first five panels of Figure 2 as discussed by (MacLeod et al. 2016; Lawrence et al. 2016; Graham et al. 2017; MacLeod et al. 2016).

One possible explanation is a change of dust extinction, such as obscuration effect by moving dust clouds as discussed by LaMassa et al. (2015) for the TDE candidate of SDSS J0159. Here, the effects of change in dust extinction in SDSS J0001 are simply discussed as follows through the python package of dust_extinction⁶. First, we assume that there is no dust extinction at the peak luminosity and that varying dust extinctions lead to the subsequent variability of light curve. Based on the SDSS i -band light curve, we can obtain the

$E(B-V)$ values of dust extinctions between two near epochs, as shown by the blue curve in left panel of Figure 11. If accepted change in dust extinction to explain the flare shown in left panel of Figure 11 in SDSS J0001, the $E(B-V)$ values could be totally same in the other bands. However, as shown in left panel in Figure 11, the same $E(B-V)$ values applied in SDSS g -band (red solid line) can lead to different variability from the observational results (black dot line). Specifically, the observed light curve is substantially higher than predicted in a scenario where dust extinction alone is responsible for the light curve state change, which implies that the observed photometric variability is not only caused by change in dust extinction. Throughout this process, the dust extinction curve of F99 is adopted (Fitzpatrick 1999). Meanwhile, we have checked other extinction curves listed in the dust_extinction package and obtained similar results.

Another possibility for explaining the light curves of SDSS J0001 is the microlensing by one or multiple foreground stars. We used the open-source microlens light curve analysis tool, *MulensModel*, to describe the SDSS g -band light curve of SDSS J0001 accepted one point source binary lens model (1S2L) in *MulensModel*. The fitting results are shown in the right panel of Figure 11. However, considering totally similar magnification factors in different optical bands in microlensing model, there should be very similar variability profiles in different bands, which is against the results shown in the first five panels of Figure 2 with much wider variability profile in the i -band than the other SDSS bands. Therefore, the microlensing

⁶ <https://dust-extinction.readthedocs.io/en/stable/index.html>

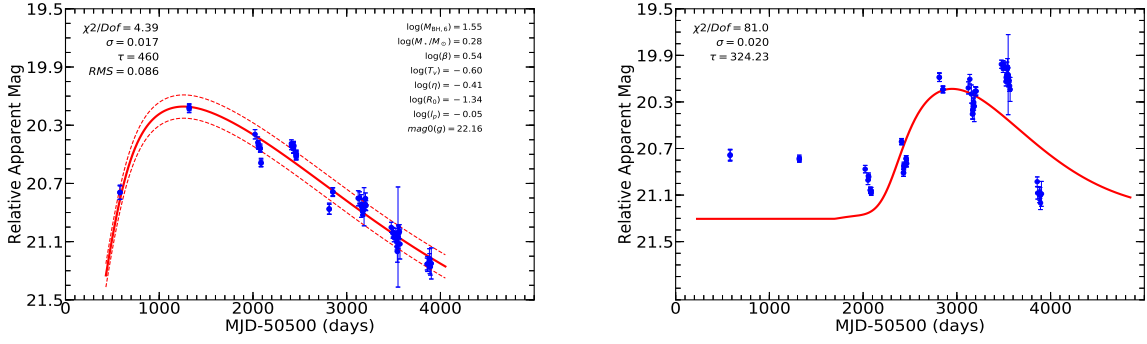


Figure 10. Examples of mock light curves generated by the CAR process model that pass (left panel) and do not pass (right panel) the criterion for evaluating whether the light curves can be fitted with the TDE model, i.e. $\chi^2/\text{dof} < 4.5$. The red solid and dashed lines represent the best TDE model fit and the corresponding RMS as determined by the kmpfit by the kmpfit. The parameters of the CAR process model for generating the mock light curves and the parameter of the TDE model are marked in each panel.

model should be not totally preferred in SDSS J0001, unless there were very distinct structures of emission regions for the SDSS *ugriz*-band emissions in SDSS J0001.

In addition, accretion can be considered to explain the light curves of SDSS J0001. On the one hand, several possible accretion models were discussed in MacLeod et al. (2016), but most predict longer timescales ($\sim 10^4$ years), which do not match the timescale observed for SDSS J0001. It cannot be ruled out that some kind of rare eruptive accretion could explain the variability of SDSS J0001, but it is hard to judge without more detailed models. Meanwhile, many studies have shown that AGN variability can be simulated using the DRW/CAR process and is considered to represent that produced by accretion. In this manuscript, we find only a 0.009% probability that the long-term variability in SDSS J0001 is due to central AGN accretion.

6 SUMMARY AND CONCLUSIONS

We have presented observational and theoretical analyses with the TDE model to a high- z ($z = 1.404$) TDE candidate in SDSS J0001, which is a quasar with apparent broad Mg II emission line. We obtained its nine-year (MJD 51082 to 54402) photometric *ugriz*-band light curves from the SDSS Stripe82 and the PHOTOOBJALL databases. It is found that the long-term variability of SDSS J0001 can be described by the conventional TDE model. We summarize our analyses as follows.

- The long-term variability of SDSS J0001 illustrates as a clear rise-to-peak followed by a smooth decline. The light curves can be fitted with the phenomenological TDE models.

- The *ugriz*-band light curves of SDSS J0001 can be described by the conventional TDE model with a main-sequence star of $M_{\star} \sim 1.905^{+0.023}_{-0.009} M_{\odot}$ tidally disrupted by central BH with $M_{\text{BH}} \sim 6.5^{+3.5}_{-2.6} \times 10^7 M_{\odot}$. Our analysis shows that the extremely long variability timescale of the SDSS J0001 is due to its high impact parameter, large masses of the central BH and the large stellar mass, and the time-dilation effect due to its high- z nature.

- Since the long-term variability has been detected in a quasar, we examine whether the variability results from AGN activity. Through the CAR process applied to create 10^5 mock light curves to trace intrinsic AGN activities, the probability of such a long-term variability being from a central AGN activity is 0.009%. Alternative

explanations for the long-term variability, including dust extinction and microlensing, are also discussed.

- The estimated virial BH mass through the broad Mg II emission line in SDSS J0001 is 7.5 times larger than that derived from our analysis. It is possible that the TDE fallback accreting debris makes a significant contribution to the Mg II emission clouds.

Based on our analysis, we suggest that there is a high-redshift TDE candidate in the quasar SDSS J0001. This provides a clue that TDEs can be detected in broad-line AGNs as well as in quiescent galaxies.

ACKNOWLEDGEMENTS

We gratefully acknowledge the anonymous referee for giving us constructive comments and suggestions to greatly improve our paper. We sincerely thank the developer of MulensModel, Dr. Radek Poleski, for friendly discussions on running this package in the Win platform. We thank Xiao Li, Xinzhe Wang, Qi Zheng, and Xiaoyan Li for useful discussion. This work is supported by the National Natural Science Foundation of China (grants NSFC-12173020, 12373014 and 12133003). Gu gratefully thank the kind financial support from the Innovation Project of Guangxi Graduate Education. The paper has made use of the code of TDEFIT <https://tde.space/tdefit/> which is a piece of open-source software written by James Guillochon for the purposes of model-fitting photometric light curves of tidal disruption events and also made use of the code of MOSFIT (Modular Open Source Fitter for Transients) <https://mosfit.readthedocs.io/> which is a Python 2.7/3.x package for fitting, sharing, and estimating the parameters of transients via user-contributed transient models. The paper has made use of the MCMC code <https://emcee.readthedocs.io/en/stable/index.html>, and made use of the Kmpfit module in Python package Kaptelyn <https://www.astro.rug.nl/software/kaptelyn/kmpfittutorial.html>.

DATA AVAILABILITY

The data underlying this article will be shared on reasonable request to the corresponding author (xgzhang@gxu.edu.cn).

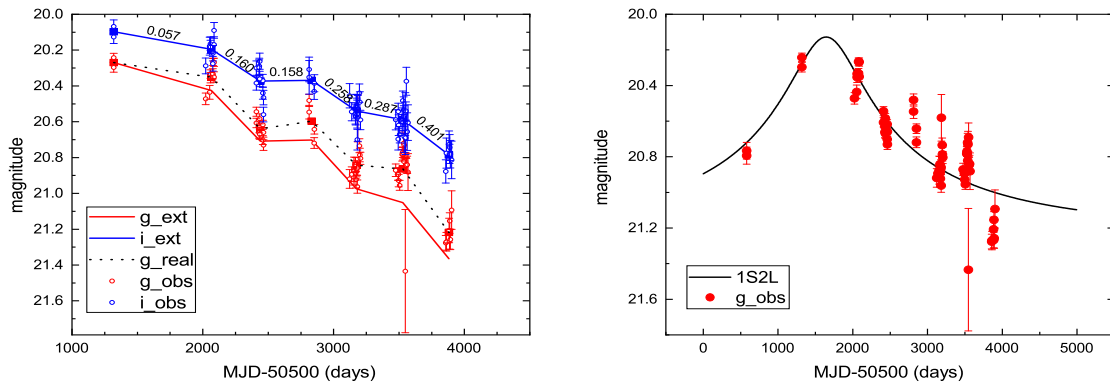


Figure 11. *Left panel*— The dust extinction effect on the *g*-band (red open circles) and *i*-band (blue open circles) data of SDSS J0001. The solid blue (or red) squares represent the average values of the *i*-band (*g*-band) magnitude in the following bins with zero time at MJD-50500: [1000, 1500], [1500, 2200], [2200, 2600], [2600, 3000], [3000,3300], [3300,3700], and [3700, 4000]. The blue solid squares from the *i*-band light curve are applied to determine $E(B-V)$ values between two epochs, marked as black characters above the solid blue line which is applied to linearly connect the blue solid squares. The solid red line shows the expected light curve through the excitation effects with applications of the same $E(B-V)$ values from the *i*-band light curve. The right panel shows the best-fitting results (black solid line) to the *g*-band light curve with the 1S2L model.

REFERENCES

- Ahumada R., et al., 2020, *ApJS*, 249, 3
Almeida A., et al., 2023, *ApJS*, 267, 44
Anderson M. M., et al., 2020, *ApJ*, 903, 116
Andrae R., Kim D. W., Bailer-Jones C. A. L., 2013, *A&A*, 554, A137
Andreoni I., et al., 2022, *Nature*, 612, 430
Arcavi I., et al., 2014, *ApJ*, 793, 38
Bade N., Komossa S., Dahlem M., 1996, *A&A*, 309, L35
Bellm E. C., et al., 2019, *PASP*, 131, 018002
Blanchard P. K., et al., 2017, *ApJ*, 843, 106
Blanton M. R., et al., 2017, *AJ*, 154, 28
Bloom J. S., et al., 2011, *Science*, 333, 203
Bramich D. M., et al., 2008, *MNRAS*, 386, 887
Brown G. C., Levan A. J., Stanway E. R., Tanvir N. R., Cenko S. B., Berger E., Chornock R., Cucchiara A., 2015, *MNRAS*, 452, 4297
Brown J. S., Shappee B. J., Holoiën T. W. S., Stanek K. Z., Kochanek C. S., Prieto J. L., 2016, *MNRAS*, 462, 3993
Brown J. S., et al., 2018, *MNRAS*, 473, 1130
Burrows D. N., et al., 2011, *Nature*, 476, 421
Campana S., Mainetti D., Colpi M., Lodato G., D’Avanzo P., Evans P. A., Moretti A., 2015, *A&A*, 581, A17
Cappelluti N., et al., 2009, *A&A*, 495, L9
Carter B., Luminet J. P., 1983, *A&A*, 121, 97
Cenko S. B., et al., 2012, *ApJ*, 753, 77
Cenko S. B., et al., 2016, *ApJ*, 818, L32
Chambers K. C., 2007, in American Astronomical Society Meeting Abstracts. p. 142.06
Chornock R., et al., 2014, *ApJ*, 780, 44
Cikota A., Leloudas G., Bulla M., Dai L., Maund J., Andreoni I., 2023, *ApJ*, 943, L18
De Colle F., Lu W., 2020, *New Astron. Rev.*, 89, 101538
Dittmann A. J., Miller M. C., 2020, *MNRAS*, 493, 3732
Donley J. L., Brandt W. N., Eracleous M., Boller T., 2002, *AJ*, 124, 1308
Drake A. J., et al., 2009, *ApJ*, 696, 870
Drake A. J., et al., 2011, *ApJ*, 735, 106
Elvis M., et al., 1994, *ApJS*, 95, 1
Esquej P., Saxton R. D., Freyberg M. J., Read A. M., Altieri B., Sanchez-Portal M., Hasinger G., 2007, *A&A*, 462, L49
Esquej P., et al., 2008, *A&A*, 489, 543
Fitzpatrick E. L., 1999, *PASP*, 111, 63
Foreman-Mackey D., Hogg D. W., Lang D., Goodman J., 2013, *PASP*, 125, 306
Frieman J. A., et al., 2008, *AJ*, 135, 338
Gezari S., 2021, *ARA&A*, 59, 21
Gezari S., et al., 2008, *ApJ*, 676, 944
Gezari S., et al., 2012, *Nature*, 485, 217
Graham M. J., Djorgovski S. G., Drake A. J., Stern D., Mahabal A. A., Glikman E., Larson S., Christensen E., 2017, *MNRAS*, 470, 4112
Greiner J., Schwarz R., Zharikov S., Orio M., 2000, *A&A*, 362, L25
Gromadzki M., et al., 2019, *A&A*, 622, L2
Grupe D., Thomas H. C., Leighly K. M., 1999, *A&A*, 350, L31
Guillochon J., Ramirez-Ruiz E., 2013, *ApJ*, 767, 25
Guillochon J., Manukian H., Ramirez-Ruiz E., 2014, *ApJ*, 783, 23
Guillochon J., Nicholl M., Villar V. A., Mockler B., Narayan G., Mandel K. S., Berger E., Williams P. K. G., 2017, MOSFIT: Modular Open-Source Fitter for Transients, Astrophysics Source Code Library, record ascl:1710.006 (ascl:1710.006)
Guillochon J., Nicholl M., Villar V. A., Mockler B., Narayan G., Mandel K. S., Berger E., Williams P. K. G., 2018, *ApJS*, 236, 6
Hammerstein E., et al., 2023, *ApJ*, 942, 9
Hinkle J. T., et al., 2023, *MNRAS*, 519, 2035
Holoiën T. W. S., et al., 2014, *MNRAS*, 445, 3263
Holoiën T. W. S., et al., 2016, *MNRAS*, 455, 2918
Holoiën T. W. S., et al., 2019, *ApJ*, 880, 120
Hung T., et al., 2017, *ApJ*, 842, 29
Hung T., et al., 2019, *ApJ*, 879, 119
Hung T., et al., 2020, *ApJ*, 903, 31
Ivanov P. B., Novikov I. D., 2001, *ApJ*, 549, 467
Kajava J. J. E., Giustini M., Saxton R. D., Miniutti G., 2020, *A&A*, 639, A100
Kelly B. C., Bechtold J., Siemiginowska A., 2009, *ApJ*, 698, 895
Kesden M., 2012, *Phys. Rev. D*, 85, 024037
Kobayashi S., Laguna P., Phinney E. S., Mészáros P., 2004, *ApJ*, 615, 855
Kochanek C. S., 1994, *ApJ*, 422, 508
Komossa S., Bade N., 1999, *A&A*, 343, 775
Komossa S., Greiner J., 1999, *A&A*, 349, L45
Komossa S., et al., 2008, *ApJ*, 678, L13
Kormendy J., Gebhardt K., 2001, in Wheeler J. C., Martel H., eds, American Institute of Physics Conference Series Vol. 586, 20th Texas Symposium on relativistic astrophysics. pp 363–381 (arXiv:astro-ph/0105230), doi:10.1063/1.1419581
Kormendy J., Ho L. C., 2013, *ARA&A*, 51, 511
Kozłowski S., 2017, *A&A*, 597, A128
Kozłowski S., et al., 2010, *ApJ*, 708, 927
Krumholz M. R., Klein R. I., McKee C. F., Offner S. S. R., Cunningham A. J., 2009, *Science*, 323, 754
LaMassa S. M., et al., 2015, *ApJ*, 800, 144
Law N. M., et al., 2009, *PASP*, 121, 1395
Lawrence A., et al., 2016, *MNRAS*, 463, 296
Leloudas G., et al., 2016, *Nature Astronomy*, 1, 0002

Levan A. J., et al., 2011, *Science*, 333, 199

Lin D., et al., 2015, *ApJ*, 811, 43

Liu X., Dittmann A., Shen Y., Jiang L., 2018, *ApJ*, 859, 8

Liu Z., Li D., Liu H.-Y., Lu Y., Yuan W., Dou L., Shen R.-F., 2020, *ApJ*, 894, 93

Lodato G., Rossi E. M., 2011, *MNRAS*, 410, 359

Lodato G., King A. R., Pringle J. E., 2009, *MNRAS*, 392, 332

MacLeod C. L., et al., 2010, *ApJ*, 721, 1014

MacLeod C. L., et al., 2012, *ApJ*, 753, 106

MacLeod C. L., et al., 2016, *MNRAS*, 457, 389

Maksym W. P., Lin D., Irwin J. A., 2014, *ApJ*, 792, L29

Markwardt C. B., 2009, in Bohlender D. A., Durand D., Dowler P., eds, *Astronomical Society of the Pacific Conference Series Vol. 411, Astronomical Data Analysis Software and Systems XVIII*. p. 251 ([arXiv:0902.2850](https://arxiv.org/abs/0902.2850)), doi:10.48550/arXiv.0902.2850

Matsumoto T., Metzger B. D., 2023, *MNRAS*, 522, 4028

Merloni A., et al., 2015, *MNRAS*, 452, 69

Mockler B., Guillochon J., Ramirez-Ruiz E., 2019, *ApJ*, 872, 151

Nolthenius R. A., Katz J. I., 1982, *ApJ*, 263, 377

Pasham D. R., et al., 2023, *Nature Astronomy*, 7, 88

Phinney E. S., 1989. p. 543

Rees M. J., 1988, *Nature*, 333, 523

Ren W., Wang J., Cai Z., Hu X., 2024, *ApJ*, 963, 7

Rhodes L., et al., 2023, *MNRAS*, 521, 389

Rosswog S., Ramirez-Ruiz E., Hix W. R., 2009, *ApJ*, 695, 404

Rumbaugh N., et al., 2018, *ApJ*, 854, 160

Ryu T., Krolik J., Piran T., 2020, *ApJ*, 904, 73

Saxton R. D., Read A. M., Komossa S., Lira P., Alexander K. D., Wieringa M. H., 2017, *A&A*, 598, A29

Saxton R., Komossa S., Auchettl K., Jonker P. G., 2021, Correction to: X-Ray Properties of TDEs, *Space Science Reviews*, Volume 217, Issue 1, article id.18 ([arXiv:2103.15442](https://arxiv.org/abs/2103.15442)), doi:10.1007/s11214-020-00759-7

Sazonov S., et al., 2021, *MNRAS*, 508, 3820

Shappee B. J., et al., 2014, *ApJ*, 788, 48

Shen Y., et al., 2011, *ApJS*, 194, 45

Sheng X., Ross N., Nicholl M., 2022, *MNRAS*, 512, 5580

Shu X. W., Wang S. S., Dou L. M., Jiang N., Wang J. X., Wang T. G., 2018, *ApJ*, 857, L16

Stone N. C., Metzger B. D., 2016, *MNRAS*, 455, 859

Stone N. C., Kesden M., Cheng R. M., van Velzen S., 2019, *General Relativity and Gravitation*, 51, 30

Tanvir N. R., et al., 2022, GRB Coordinates Network, 31602, 1

Tonry J. L., et al., 2018, *PASP*, 130, 064505

Tout C. A., Pols O. R., Eggleton P. P., Han Z., 1996, *MNRAS*, 281, 257

Trakhtenbrot B., et al., 2019a, *Nature Astronomy*, 3, 242

Trakhtenbrot B., et al., 2019b, *ApJ*, 883, 94

Udalski A., Szymański M. K., Szymański G., 2015, *Acta Astron.*, 65, 1

Wang X.-Y., Liu R.-Y., 2016, *Phys. Rev. D*, 93, 083005

Wevers T., et al., 2019, *MNRAS*, 488, 4816

Wyrzykowski L., et al., 2014, *Acta Astron.*, 64, 197

Wyrzykowski L., et al., 2017, *MNRAS*, 465, L114

Yan Z., Xie F.-G., 2018, *MNRAS*, 475, 1190

Yang C.-W., Wang T.-G., Ferland G., Yuan W., Zhou H.-Y., Jiang P., 2013, *ApJ*, 774, 46

Yang C., Wang T., Ferland G. J., Dou L., Zhou H., Jiang N., Sheng Z., 2017, *ApJ*, 846, 150

Yao Y., et al., 2023, *ApJ*, 955, L6

Yao Y., Lu W., Harrison F., Kulkarni S. R., Gezari S., Guolo M., Cenko S. B., Ho A. Y. Q., 2024, *ApJ*, 965, 39

Zhang X.-G., 2021, *MNRAS*, 500, L57

Zhang X.-G., 2022, *MNRAS*, 516, L66

Zhang X., 2023, arXiv e-prints, p. arXiv:2310.07095

Zhang X.-G., Bao M., Yuan Q., 2019, *MNRAS*, 490, L81

Zhang X., YingFei Z., PeiZhen C., BaoHan W., Yi-Li L., HaiChao Y., 2021, *ApJ*, 922, 248

Zhang W. J., et al., 2022, *A&A*, 660, A119

Zu Y., Kochanek C. S., Kozłowski S., Udalski A., 2013, *ApJ*, 765, 106

Zu Y., Kochanek C. S., Kozłowski S., Peterson B. M., 2016, *ApJ*, 819, 122

van Velzen S., et al., 2011, *ApJ*, 741, 73

van Velzen S., et al., 2019, *ApJ*, 872, 198

van Velzen S., et al., 2021, *ApJ*, 908, 4

7 APPENDIX

7.1 Appendix A: SQL search

According to the multi-epoch objids related to the THINGID=107540835 for SDSS J0001, the detailed query in SQL⁷ search is as follows:

```
select mjd, psfmag_u, psfmagerr_u, psfmag_g, psfmagerr_g, psf-
mag_r, psfmagerr_r, psfmag_i,
psfmagerr_i, psfmag_z, psfmagerr_z
from PHOTOOBJALL
where
objid = 1237663277927891217 or objid=1237663479807475923
or objid=1237663527055327473 or objid=1237663716014489812
or objid=1237663784734425357 or objid=1237666649495699593
or objid=1237667173463163111 or objid=1237646012157001880
or objid=1237653012973486327 or objid=1237659756054577365
or objid=1237659906395013297 or objid=1237660026651410679
or objid=1237660224222068977 or objid=1237660357358125285
```

7.2 Appendix B: An example linear interpolation processes

Figure B1 shows examples of our calculations for $\dot{M}_a(T_v, \beta)$ by adopting some parameter sets of $\{T_v, \beta\}$.

This paper has been typeset from a $\text{\TeX}/\text{\LaTeX}$ file prepared by the author.

⁷ <https://skyserver.sdss.org/dr16/en/tools/search/sql.aspx>

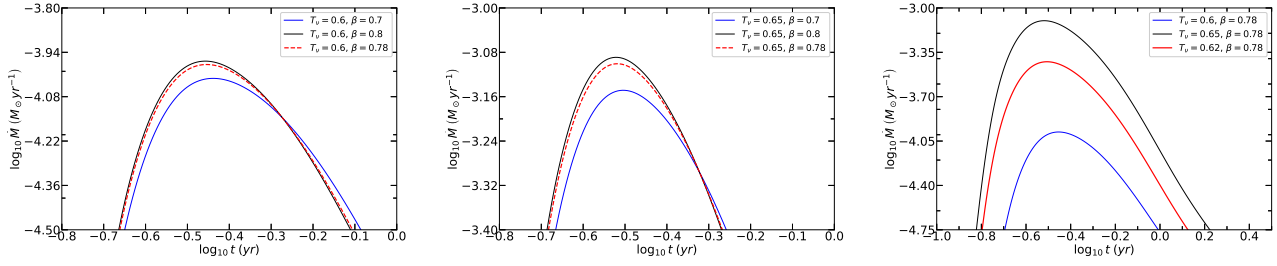


Figure B1. The intuitive schematic diagram of the interpolation process. In the left panel, the solid green lines represent results for $\dot{M}_a(T_v = 0.6, \beta = 0.7)$ and $\dot{M}_a(T_v = 0.6, \beta = 0.8)$ included in the template, and the dashed red line shows the interpolation results for $\dot{M}_a(T_v = 0.6, \beta = 0.78)$ derived from the first sub-equation in Equation (3). In the middle panel, the solid green lines show the results for $\dot{M}_a(T_v = 0.65, \beta = 0.7)$ and $\dot{M}_a(T_v = 0.65, \beta = 0.8)$ included in the template, and the dashed red line shows the interpolation results for $\dot{M}_a(T_v = 0.65, \beta = 0.78)$ from the second sub-equation in Equation (3). In the right panel, the solid green lines show the interpolation results for $\dot{M}_a(T_v = 0.6, \beta = 0.78)$ and $\dot{M}_a(T_v = 0.65, \beta = 0.78)$ shown as dashed red lines in the left and middle panels. The solid red line shows the interpolation results for $\dot{M}_a(T_v = 0.62, \beta = 0.78)$ by the Equation (4).